Received: 20 November 2019 | Revised: 20 December 2019 | Accepted: 23 December 2019

DOI: 10.1002/eom2.12013

RESEARCH ARTICLE

EcoMat FUNCTIONAL MATERIALS FOR GREEN ENERGY AND ENVIRONMENT WILEY

Metal-free graphene/boron nitride heterointerface for CO_2 reduction: Surface curvature controls catalytic activity and selectivity

Xin Mao[1] | Dimuthu Wijethunge[1] | Lei Zhang[1] | Sufan Wang[2] | Cheng Yan[1] | Zhonghua Zhu[3] | Aijun Du[1]

[1]School of Chemistry, Physics and Mechanical Engineering, Science and Engineering Faculty, Queensland University of Technology, Brisbane, Australia

[2]College of Chemistry and Materials Science, Anhui Normal University, Wuhu, China

[3]School of Chemical Engineering, University of Queensland, Brisbane, Australia

Correspondence
Aijun Du, School of Chemistry, Physics and Mechanical Engineering, Science and Engineering Faculty, Queensland University of Technology, Gardens Point Campus, Brisbane, QLD 4000, Australia.
Email: aijun.du@qut.edu.au

Funding information
Australian Research Council under Discovery Project, Grant/Award Numbers: DP170104660, DP170103598

Abstract

Searching environmentally friendly and low-cost catalysts for CO_2 reduction is critical for the development of sustainable energy and environmental technologies. In this work, we report a novel heterointerface between graphene and BN nanotubes or nanoribbons as efficient catalysts for CO_2 reduction with high activity and selectivity. The active sites are found to be at the C-N interfaces of graphene-BN (G-BN) and their excellent catalytic performance is derived from the surface curvature effect. The density functional theory (DFT) results reveal that the most energy favorable pathway for the formation of CH_3OH is $* + CO_2 \rightarrow *COOH \rightarrow *CO \rightarrow *OCH \rightarrow *OCH_2 \rightarrow *OCH_3 \rightarrow *CH_3OH \rightarrow * + CH_3OH$. And the formation of CH_4 is through $* + CO_2 \rightarrow *COOH \rightarrow *CO \rightarrow *OCH \rightarrow *OCH_2 \rightarrow *OCH_3 \rightarrow *O + CH_4 \rightarrow *OH + CH_4 \rightarrow *H_2O + CH_4$ pathway. Moreover, the calculated results further demonstrate that for the smaller index of G-BN nanotubes, such as G-BN (3), the formation of CH_3OH product is much easier than the *O intermediate and CH_4 molecule due to the lower free energy change. However, for the higher indexed G-BN nanotubes, after forming $*OCH_3$ intermediate, the generation of *O and CH_4 molecule is more feasible, particularly for G-BN (9), and the calculated limiting potential is only −0.42 V, which is higher than the best Cu-based materials, like −0.93 V on Cu(111), and −0.74 V on Cu (211). This metal free heterostructure is confirmed to facilitate CO_2 conversion with high activity and selectivity, demonstrating a great potential as a new type of catalyst for CO_2 reduction.

KEYWORDS

CO_2 reduction, first-principles calculation, heterostructures, limiting potentials, metal-free catalysts

1 | INTRODUCTION

Electrochemical CO_2 reduction into hydrocarbon fuels and chemicals is one of the most challenging task in the field of chemistry, which is normally limited by the activity and selectivity of the catalysts.[1,2] To date, most reported catalysts are based on transition metals (TM) or their oxides, dichalcogenides, and alloys.[3-7] So far, limited work using metal-free materials have been reported. However, compared to TM atoms, metal-free catalysts have the advantages of being cheap, and environmentally friendy.[8] Under the mild conditions, metal-free catalysts also exhibit a high activity and selectivity to some chemical reactions, such as water splitting, fuel cells, and N_2 fixation processes.[9-15]

As a typical two-dimensional (2D) metal-free material, pure graphene and BN have been wildly investigated due to their fascinating physical and chemical properties.[16] However, since the free flowing of π electrons of sp^2 carbon materials and large band gap of BN, they are inert for many chemical reactions. Whereas, doping metal atoms and nonmetal atoms into the basal plane of pristine graphene and BN can significantly enhance the reaction activity, particularly in certain catalytic processes.[17,18] For example, B-doped graphene has been applied as a metal-free catalyst for N_2 fixation with a low overpotential.[19] A series of N-doped graphene materials have been realized in many electrocatalytic reactions, such as oxygen evolution reaction (OER), oxygen reduction reaction (ORR), and CO_2 reduction reaction.[20-22] These dopants and their doping methods play a significant role in catalyzing chemical reactions, compared to two disparate materials.[16,23] Hybrid graphene-BN (G-BN) nanomaterials with armchair G-BN interface, B-C zigzag interface, and N-C zigzag interface have been successfully synthesized in laboratory.[24,25] However, the investigation of their potential in some chemical processes have been rarely studied.

In this work, by using first-principles calculations, we have designed a series of G-BN nanotubes with different index from (3) to G-BN (9), and G-BN nanoribbons for CO_2 reduction reactions (CRR). According to the band decomposed charge density, the intrinsic catalytic mechanism originates from the high activity C-N interface as the active site during the CO_2 reduction process. As one main side reaction, the comparison of hydrogen evolution reactions (HER) activity with CRR is necessary. By comparing the binding effect of *COOH and *H intermediates, we found that all G-BN nanotubes and nanoribbons prefer to produce *COOH due to the lower binding energy than *H, thus HER is highly suppressed on these catalysts. We also observed that the binding energy of *COOH is linear with the index of G-BN nanotubes, indicating that the change in surface curvature helps predict the best CO_2 electrocatalysts. Based on this, we have investigated the catalytic performance of the formation of two main value-added chemicals, CH_3OH and CH_4. DFT calculation results showed that CH_3OH can be generated on G-BN (3) nanotube with a limiting potential of −0.88 V. However, for higher indexed G-BN nanotubes, like G-BN (9) exhibits high catalytic activity to reduce CO_2 into CH_4 with a limiting potential of only −0.42 V, which is higher than Cu-based materials, such as −0.93 V on Cu(111), and −0.74 V on Cu (211).[26,27]

2 | RESULTS AND DISCUSSION

2.1 | Structures of G-BN nanoribbons and nanotubes

Figure 1 presents the optimized structures of G-BN armchair nanoribbons and nanotubes. G-BN heterostructures can be regarded as the combination of zigzag graphene and zigzag BN, which have the similar crystal structures and lattice constants (only 1.8% mismatch).[28,29] After the combination of graphene and BN, G-BN nanomaterials exhibit some unique characteristics, such as band gap opening, excellent thermal transport, and intrinsic half-metallic behavior.[16,30] For the G-BN armchair nanotubes, previous works have proved that the smallest nanotube which can be constructed is G-BN (3).[31] And with the increase of the index of G-BN nanotubes, the properties of G-BN nanotubes become similar to the G-BN nanoribbon. Thus, in this work, we only consider the index of G-BN nanotubes starts from (3) to (9) and the G-BN nanoribbon. Band structures and band decomposed

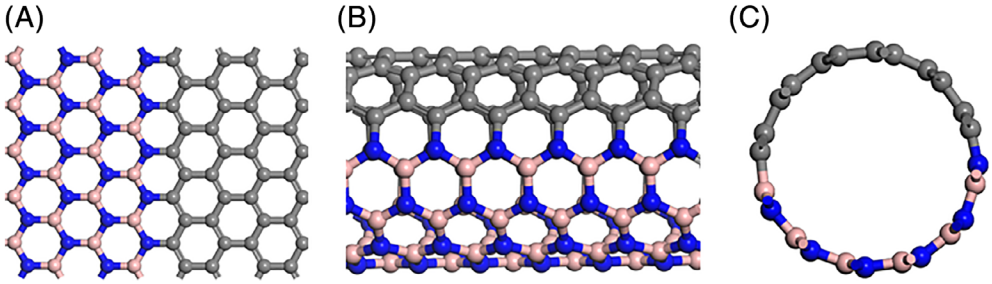

FIGURE 1 (A) The optimized structure for G-BN nanoribbon. (B), (C) The top view and side view for G-BN nanotube take G-BN (6) for an example. The grey, pink, and blue balls represent the C, B, and N atoms

charge density of G-BN nanoribbon and nanotube have been plotted in Figure 2. From the band structures, a good conductivity of G-BN nanotubes and nanoribbons can be observed, suggesting the high potential in catalyzing CO_2. Moreover, the wave functions of valence bond maximum (VBM) and conduction bond minimum (CBM) are mainly originated from the hybridization p orbitals among C, B, and N atoms. Due to the lower energy of $\pi_{C\text{-}B}$ orbital than that of the $\pi^*_{C\text{-}N}$ orbital, the VBM around the Fermi level stems from the $\pi_{C\text{-}B}$ orbitals along the C-B interface. On the other hand, the CBM contributed from the $\pi^*_{C\text{-}N}$ orbitals along the C-N interface, demonstrating the high conductivity and activity of C-N interface. Based on this point, only C-N interface is designed as the active site for the adsorption and reduction of CO_2 molecules, which is in good agreement with previous reports.[16] To further identify the active site along the C-N interface, the binding energies of *COOH on B site and N site have been tested as shown in Table S2. The calculated results suggest that the adsorption on B site is much stronger due to the lower binding energy. Therefore, only B site is designed to be active site in the subsequent CO_2 reduction process.

2.2 | Suppressing HER and curvature effects

The evolution of hydrogen is one main side reaction of CO_2 reduction process. Therefore, it is necessary to investigate and compare the activity of HER and CRR in the catalysts. Since the competition between CRR and HER is mainly determined by the stability of the first hydrogenated intermediates, thus, the formation of *COOH and *H on the catalysts is investigated and the optimized structures are presented in Figure 3. If the *COOH intermediate is more stable than the *H species, then HER process will be suppressed, otherwise, H atom can occupy the active site before CO2RR starts. For G-BN nanoribbon, the binding energy of *H and COOH* is −0.147 and −0.266 eV, respectively. For G-BN nanotubes, the binding energies of *H and *COOH to G-BN (3) are −0.215, and −0.89 eV, respectively. And these binding energies increase with the index of G-BN nanotubes. For example, the binding energies of *H and *COOH for G-BN (9) are 0.127 and −0.274 eV, which is very close to the G-BN nanoribbon. We also calculated the Gibbs free energy changes of these two intermediates for comparison as shown in Figure 3. Clearly, the formation of *COOH is much favorable than *H group for all of the G-BN nanomaterials, demonstrating the high selectivity to produce *COOH rather than *H. Moreover, from G-BN (3) to G-BN (9), the free energy changes show an increasing trend, and finally reach to the value of G-BN nanoribbon structure, suggesting that by tuning surface curvature, efficient CO_2 reduction can be achieved.

Based on the discussion above, the different curvature effects of G-BN nanotubes exhibit diverse adsorption energies of *COOH and *H. We further examined the surface curvature effects on the reduction performance of CO_2 molecules. Except for the strong binding effect of *COOH, the appropriate binding energy between $*OCH_3$ and catalysts also plays a significant role in reducing CO_2, as the weak interaction of $*OCH_3$ helps remove the reaction products. Therefore, a good CO_2 reduction catalyst needs to meet two criteria. On one hand, the strong binding effect with the *COOH to make sure efficient capturing of the reactant and HER suppression. On the other hand, the weak interaction with $*OCH_3$ to make

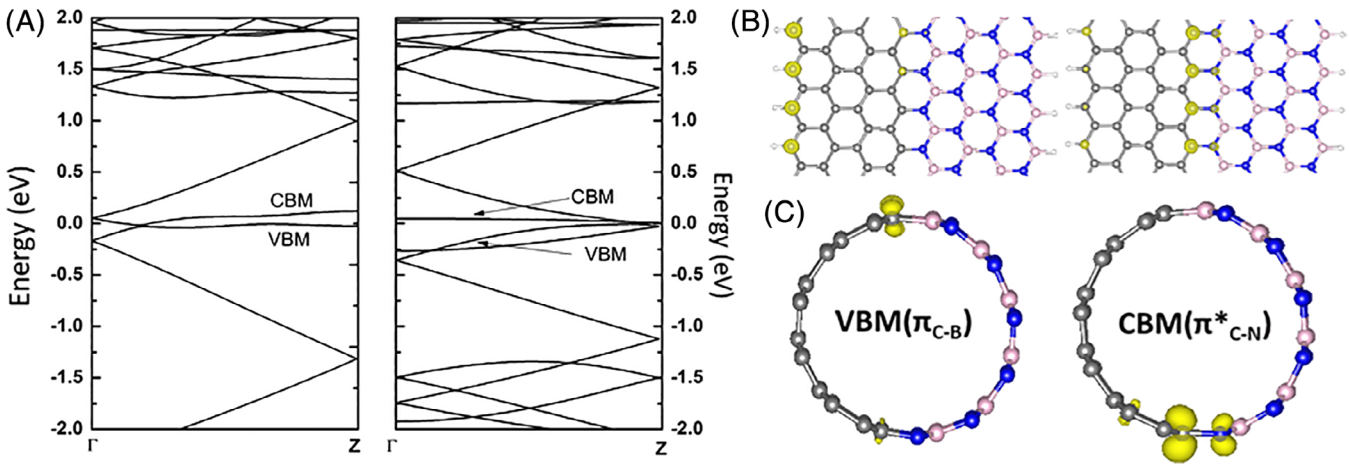

FIGURE 2 (A) The band structures for the G-BN nanoribbon and G-BN (6) nanotube. (B). The valence bond maximum and conduction bond minimum of G-BN nanoribbon and nanotubes. The iso-surface value is 0.05 e $Å^{-3}$. The grey, pink, blue, and white balls represent the C, B, N, and H atoms

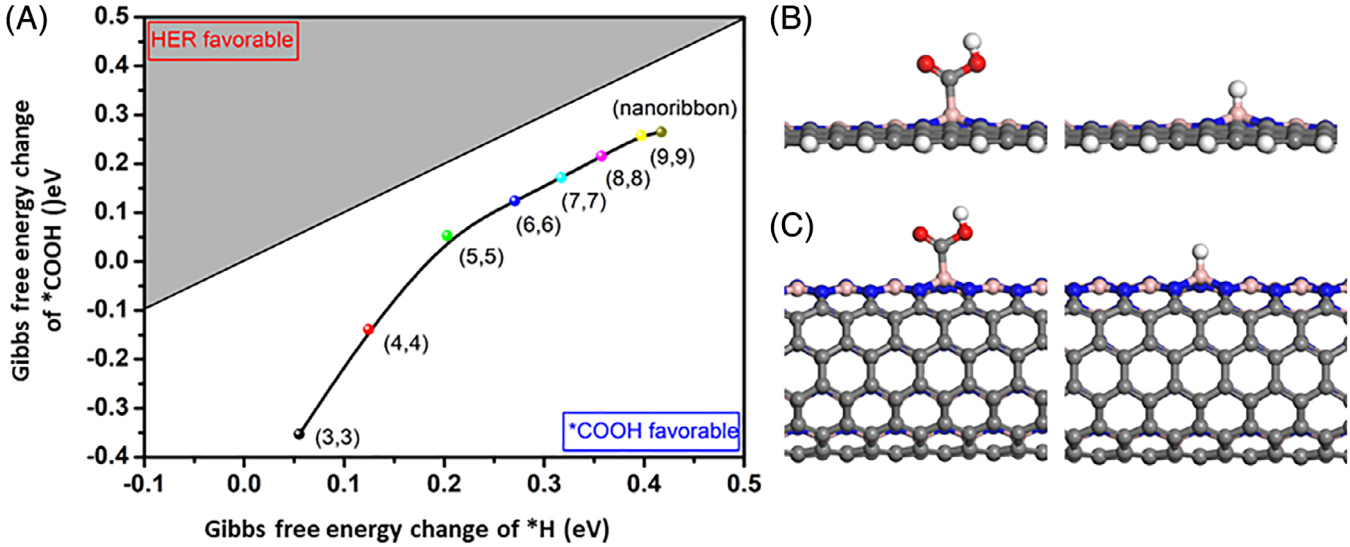

FIGURE 3 (A) Comparison of hydrogen evolution reactions and CO_2 reduction reactions on G-BN nanoribbon and nanotubes. (B) The optimized structures for the adsorption of *COOH and *H on G-BN nanoribbon. (C) The optimized structures for the adsorption of *COOH and *H on G-BN (6) nanotube

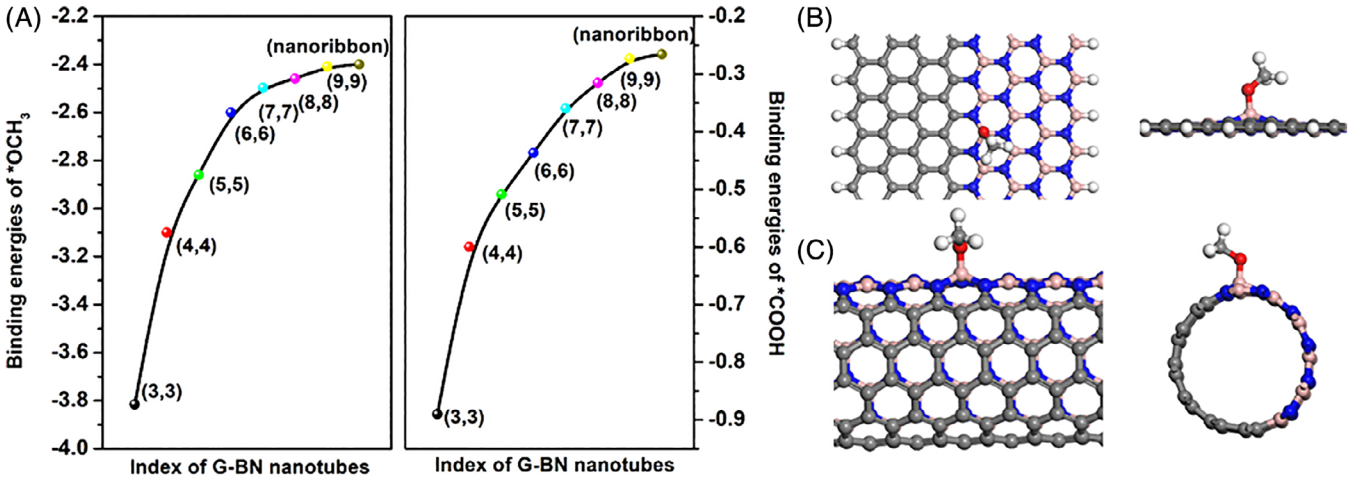

FIGURE 4 (A) Binding energies of $*OCH_3$ and *COOH on G-BN nanoribbon and nanotubes. (B) The top view and side view of the optimized structures for the adsorption of $*OCH_3$ on G-BN nanoribbon. (C) The top view and side view of the optimized structures for the adsorption of $*OCH_3$ on the G-BN (6) nanotube

the desorption step of CH_3OH easy to proceed. Figure 4 depicts the binding energies of $*OCH_3$ and *COOH on catalysts and their optimized structures. According to the figure, G-BN (3) has a strong binding effect with *COOH and $*OCH_3$, while G-BN (9) exhibits the weak interaction with these two intermediates, indicating the significant role of surface curvature in catalyzing CO_2.

2.3 | CO_2 reduction mechanisms

The generation of CO and HCOOH consist of only two proton/electron (H^+/e^- pair) transfer processes. The first hydrogenated step is the same for the formation of CO and HCOOH, and the reaction starts to diverge from the second hydrogenated step. For CO formation process, the H^+/e^- pair attacks the oxygen site of *COOH group, then *CO group produce with one water molecule releasing the system. And the last step is the desorption of CO molecule. For HCOOH formation process, the H^+/e^- pair continue attacking the C site of *COOH to produce HCOOH. Figure 5 depicts the Gibbs free energy change diagrams for the formation of these two products on the catalysts. We find that the second hydroghenated step of the formation of *HCOOH has a lower free energy change compared to the formation of *CO for eight

catalysts, demonstrating the high selectivity toward HCOOH comapred to CO molecules. Insights into the reduction CO_2 to CO molecule, for the low index of G-BN nanotubes, such as G-BN (3) to G-BN (8), is that second step is the potential determining step (PDS), and the limiting potential decreases with the increase of index number of G-BN nanotubes. For the formation of CO on G-BN (9) and G-BN nanoribbon, the first step is the PDS of the whole reduction process, this is because these two catalysts have a weak interaction with *COOH group. However, for the generation of HCOOH process, from G-BN (3) to G-BN (7), the second hydrogenated step is the PDS, and the limiting potential decreases with the index of G-BN nanotubes. For G-BN (8), G-BN (9), and G-BN nanoribbons, the first step is the PDS of the whole reduction process.

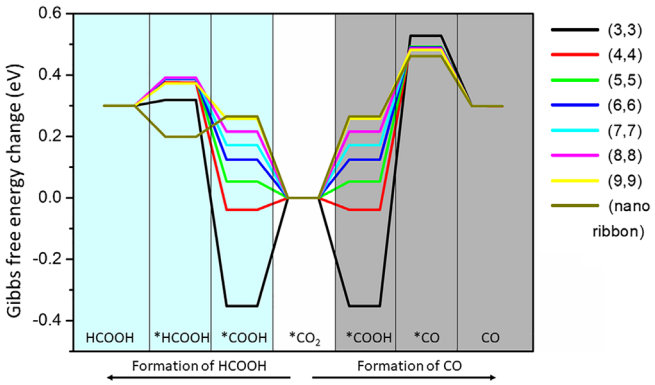

FIGURE 5 The Gibbs free energy change diagrams for the formation of CO and HCOOH molecules on the catalysts

Then, we investigate the formation of methanol and methane pathways on G-BN catalysts as shown in Figure 6 and Figure 7. As a main organic chemical raw material, the CH_3OH formation consists of six hydrogenated elementary steps. Taking G-BN (3) for an example, one CO_2 molecule first reacts with one H^+/e^- pair on the active site to produce *COOH intermediate with a free energy change of −0.35 eV. Once *COOH species is formed, it can be further hydrogenated to produce *CO intermediate with one water transferred into the electrolyte, and the free energy change of this step uphills by 0.88 eV. After that, the adsorbed *CO group will be further reduced to *OCH or *COH species by reacting with another H^+/e^- pair. By comparing the free energy change of these two elementary steps, the formation of *OCH group is energetically favorable as this process is exothermic (−0.69 eV), while the formation of *COH group can hardly happen under the ambient condition. The new

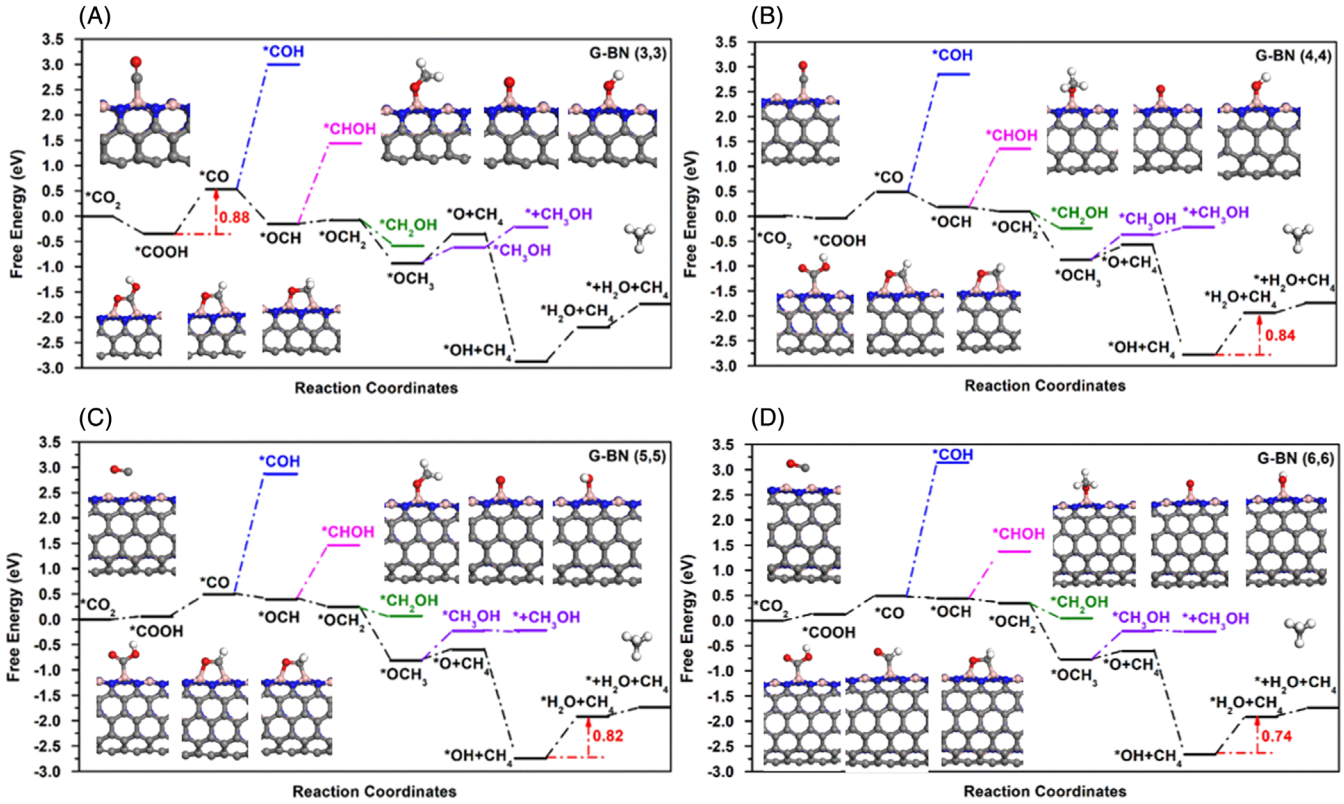

FIGURE 6 The Gibbs free energy change diagrams for the formation of CH_3OH and CH_4 on the G-BN nanoribbon and nanotubes. (A) G-BN (3), (B) G-BN (4), (C) G-BN (5) and (D) G-BN (6). The optimized structures for some main intermediates are also presented in the figure

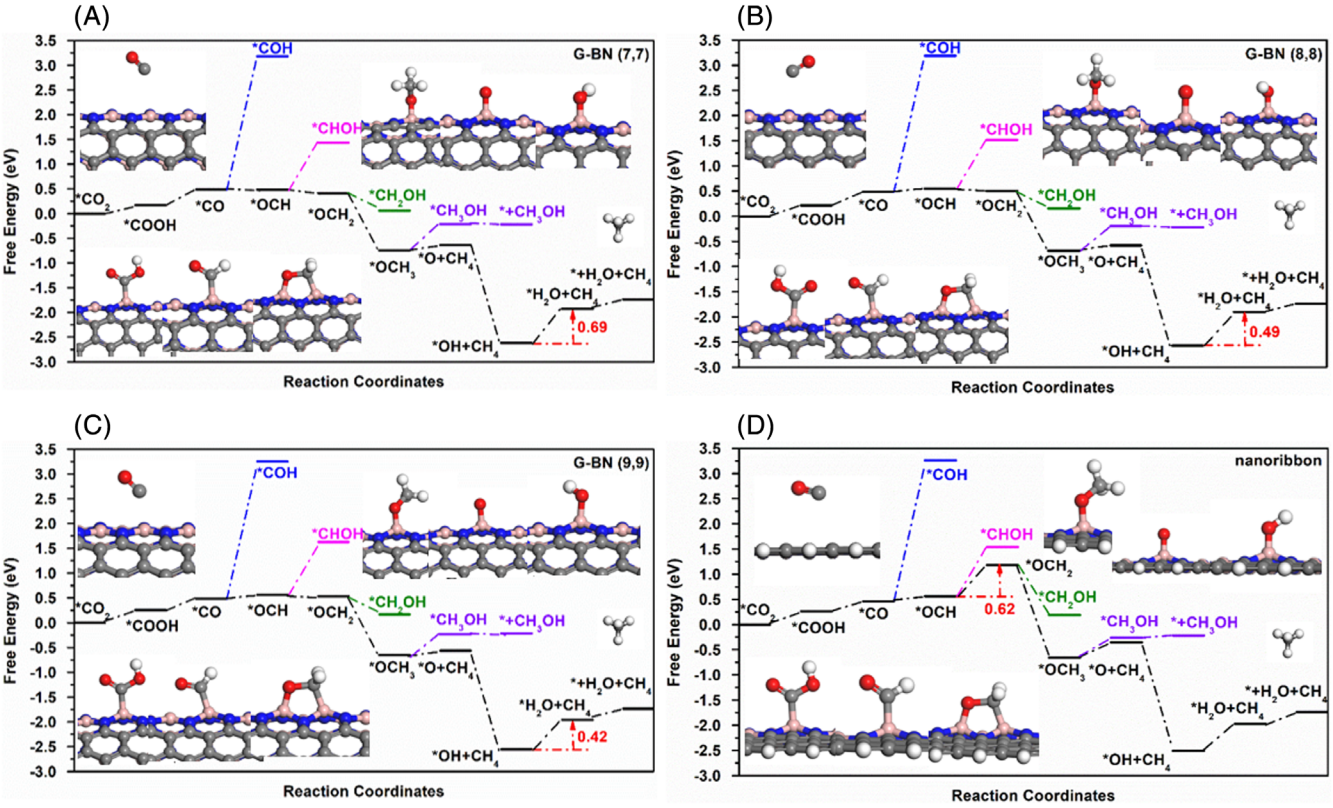

FIGURE 7 The Gibbs free energy change diagrams for the formation of CH_3OH and CH_4 on the G-BN nanoribbon and nanotubes. (A) G-BN (7), (B) G-BN (8), (C) G-BN (9) and (D) G-BN nanoribbon. The optimized structures for some main intermediates are also presented in the figure

formed *OCH group can either be reduced to $*OCH_2$ or *CHOH by interacting with the third H^+/e^- pair, and the formation of $*OCH_2$ is energetically lower than *CHOH (0.07 eV V.S. 1.60 eV). Then, the $*OCH_2$ species continually reacts with the H^+/e^- pair to form $*OCH_3$ or $*CH_2OH$, but the free energy change for the formation of $*OCH_3$ is much lower, only −0.85 eV. The final step to produce methanol on the catalyst is $*OCH_3 + H^+ + e^- \rightarrow$ *CH3OH, and the calculated free energy change uphills by 0.30 eV. When considering the product desorption on the catalyst, we find that the release of CH_3OH is also easy to proceed due to the low free energy change (0.42 eV). Based on the above results, the most favorable pathway for CO_2 reduction on G-BN (3) can be easily identified, that is, . $* + CO_2 \rightarrow *COOH \rightarrow *CO \rightarrow *OCH \rightarrow *OCH_2 \rightarrow *OCH_3 \rightarrow *CH_3OH \rightarrow * + CH_3OH$. The PDS of the whole pathway is the step of $*COOH \rightarrow *CO$ due to its maximum free energy change (0.88 eV). Furthermore, the limiting potential can also be calculated according to the computational hydrogen electrode (CHE) model, which is defined as the following equation, $UL = -\Delta G_{max}/e$, where ΔG_{max} denotes the largest free energy change of the whole pathway when reducing CO_2. Therefore, the limiting potential for reduction of CO_2 to CH_3OH on G-BN (3) is −0.88 V.

The formation of CH_4 molecules consists of eight elementary steps. And the first five steps are the same to the CH_3OH generation. After the formation of $*OCH_3$ on the catalysts, the *O is produced on the active site with one methane generated and released the system. This step is found to be energetically unfavorable on G-BN (3), however, for higher indexed G-BN nanotubes and nanoribbons, the free energy change of the generation of *O is much lower than $*CH_3OH$. For example, in G-BN (4) nanotube, the free energy change of this step only uphills by 0.30 eV. Then, the adsorbed *O group continually react with H^+/e^-pair to form *OH with the free energy change of −2.21 eV. After that the $*H_2O$ can be produced on the catalyst, and the calculated free energy is 0.84 eV for G-BN (4), which is the PDS of the whole pathway. And the removal of product is found to be much easier with free energy change of 0.20 eV. Therefore, the limiting potential of the reduction of CO_2 into CH_4 on G-BN (4) is −0.84 V. For the CO_2 reduction of other higher indexed G-BN nanotubes, like G-BN (5), G-BN (6), G-BN (7), G-BN (8), and G-BN (9). The step of $*OH \rightarrow *H_2O$ also have the maximum free energy changes, 0.82, 0.74, 0.69, 0.49, and 0.42 eV, respectively, which is also considered as the PDS process for these catalysts. For the G-BN nanoribbon, we find the step of

*OCH → *OCH_2 has the largest free energy change of 0.62 eV, thus, the limiting potential for the CO_2 conversion to CH_4 on G-BN nanoribbon is −0.62 V. Among these eight catalysts, G-BN (9) exhibits the highest catalytic performance for CO_2 reduction to CH_4 with a limiting potential of −0.42 V, which is higher than some best metal based catalysts, like −0.93 V on Cu(111), and −0.74 V on Cu (211).[26,27]

3 | CONCLUSION

By using first-principles calculations, a series of metal-free G-BN nanomaterials have been designed for the CO_2 reduction, and the C-N interface is found to be the active sites for this process. HER is suppressed on all the G-BN nanotubes and nanoribbons due to the strong binding effects with *COOH group. The surface curvature effect of G-BN nanotubes can have significant impact on the binding energies of adsorbed species including *COOH and *CH_2OH intermediates and then the best catalysts for CO_2 conversion can be screened out. Our DFT calculation results further demonstrate that for the smaller index of G-BN nanotubes, such as G-BN (3), the formation of CH_3OH product is much easier than the *O intermediate and CH_4 molecule due to the lower free energy change. However, the high index of G-BN nanotube facilitates the formation of CH_4, particular for G-BN (9), the calculated limiting potential is −0.42 V, which is higher than the best reported Cu-based materials, like −0.93 V on Cu(111), and −0.74 V on Cu (211). Our study proposes a promising metal-free catalyst with high activity and high selectivity in catalyzing the CO_2 reduction.

3.1 | Experimental Section

All spin-polarized calculations were performed by using density functional theory as implemented in the Vienna Ab-initio Simulation Package (VASP) for geometry structures optimization.[32,33] The exchange-correlation interactions were described by the generalized gradient approximation (GGA)[34] in the form of the Perdew-Burke-Ernzerhof (PBE) functional.[35] The dispersion interaction was considered by using DFT + D3 semiempirical correction in Grimme's scheme.[36] The convergence tolerances of energy, force, and displacement for the geometry optimization were set to 10^{-5} eV, and 5×10^{-3} eV/Å, and 5×10^{-3} Å, respectively. A 500 eV cut-off energy was used during the calculation. The vacuum space was set to more than 15 Å, which was enough to avoid the interaction between periodical images. Graphene/BN nanoribbon was built by using a supercell containing (5 × 5) graphene unit cell and (5 × 5) BN unit cell with the edge atoms saturated with hydrogen. For graphene/BN nanotubes, the supercell models include six unit cells for (n, 0) zigzag graphene and BN nanotubes.

The Gibbs free energy changes (ΔG) for each elementary steps were calculated based on the CHE model proposed by Norskov et al,[37,38] which is determined by the following equation:

$$\Delta G = \Delta E + \Delta ZPE - T\Delta S + \Delta G_U + \Delta G_{pH}$$

where ΔE denotes the electronic energy change directly obtained from DFT calculations, ΔZPE is the correction of zero-point energies (ZPE), T is the temperature of 298.15 K, and ΔS is the change in entropy. Table S1 shows the corrections including ZPE, and entropy for gas phase molecules and adsorbed species. $\Delta G_U = -eU$ is the contribution of electrode potential to ΔG, and $\Delta G_{pH} = -k_B T \ln 10 * pH$.

ACKNOWLEDGMENTS

We acknowledge the generous grants of high-performance computer resources provided by NCI National Facility and The Pawsey Supercomputing Centre through the National Computational Merit Allocation Scheme supported by the Australian Government and the Government of Western Australia. A. D. greatly appreciates the financial support by Australian Research Council under Discovery Project (DP170103598). A.D. and Z. Z. also thank the financial support by ARC Discovery Project DP170104660.

ORCID

Aijun Du https://orcid.org/0000-0002-3369-3283

REFERENCES

1. Jin H, Guo C, Liu X, et al. Emerging two-dimensional nanomaterials for electrocatalysis. *Chem Rev*. 2018;118:6337-6408.
2. Sun Z, Ma T, Tao H, Fan Q, Han B. Fundamentals and challenges of electrochemical CO2 reduction using two-dimensional materials. *Chem-Us*. 2017;3:560-587.
3. Asadi M, Kim K, Liu C, et al. Nanostructured transition metal dichalcogenide electrocatalysts for CO2 reduction in ionic liquid. *Science*. 2016;353:467-470.
4. Zhu W, Michalsky R, Metin O, et al. Monodisperse au nanoparticles for selective electrocatalytic reduction of CO2 to CO. *J Am Chem Soc*. 2013;135:16833-16836.
5. Kattel S, Ramírez PJ, Chen JG, Rodriguez JA, Liu P. Active sites for CO2 hydrogenation to methanol on cu/ZnO catalysts. *Science*. 2017;355:1296-1299.
6. Kattel S, Liu P, Chen JG. Tuning selectivity of CO2 hydrogenation reactions at the metal/oxide interface. *J Am Chem Soc*. 2017;139:9739-9754.
7. Zhao Z, Lu G. Computational screening of near-surface alloys for CO2 electroreduction. *Acs Catal*. 2018;8:3885-3894.

8. Chai GL, Guo ZX. Highly effective sites and selectivity of nitrogen-doped graphene/CNT catalysts for CO2 electrochemical reduction. *Chem Sci*. 2016;7:1268-1275.
9. Zhang J, Zhao Z, Xia Z, Dai L. A metal-free bifunctional electrocatalyst for oxygen reduction and oxygen evolution reactions. *Nat Nanotechnol*. 2015;10:444-452.
10. Qian Y, Hu Z, Ge X, et al. A metal-free ORR/OER bifunctional electrocatalyst derived from metal-organic frameworks for rechargeable Zn-air batteries. *Carbon*. 2017;111:641-650.
11. Wang X, Vasileff A, Jiao Y, Zheng Y, Qiao SZ. Electronic and structural engineering of carbon-based metal-free electrocatalysts for water splitting. *Adv Mater*. 2019;31:1803625.
12. Hu C, Lin Y, Connell JW, et al. Carbon-based metal-free catalysts for energy storage and environmental remediation. *Adv Mater*. 2019;31:1806128.
13. Ling C, Niu X, Li Q, Du A, Wang J. Metal-free single atom catalyst for N_2 fixation driven by visible light. *J Am Chem Soc*. 2018;140:14161-14168.
14. Mao X, Zhou S, Yan C, Zhu Z, Du A. A single boron atom doped boron nitride edge as a metal-free catalyst for N_2 fixation. *Phys Chem Chem Phys*. 2019;21:1110-1116.
15. Mao X, Kour G, Zhang L, et al. Silicon-doped graphene edges: an efficient metal-free catalyst for the reduction of CO_2 into methanol and ethanol. *Cat Sci Technol*. 2019;9:6800-6807.
16. Sun Q, Sun C, Du A, Dou S, Li Z. In-plane graphene/boron-nitride heterostructures as an efficient metal-free electrocatalyst for the oxygen reduction reaction. *Nanoscale*. 2016;8:14084-14091.
17. Mao X, Kour G, Yan C, Zhu Z, Du A. Single transition metal atom-doped graphene supported on a nickel substrate: enhanced oxygen reduction reactions modulated by electron coupling. *J Phys Chem C*. 2019;123:3703-3710.
18. Mao X, Zhang L, Kour G, et al. Defective graphene on the transition-metal surface: formation of efficient bifunctional catalysts for oxygen evolution/reduction reactions in alkaline media. *Acs Appl Mater Inter*. 2019;11:17410-17415.
19. Yu X, Han P, Wei Z, et al. Boron-doped graphene for electrocatalytic N_2 reduction. *Joule*. 2018;2:1610-1622.
20. Luo Z, Lim S, Tian Z, et al. Pyridinic N doped graphene: synthesis, electronic structure, and electrocatalytic property. *J Mater Chem*. 2011;21:8038-8044.
21. Qu L, Liu Y, Baek JB, Dai L. Nitrogen-doped graphene as efficient metal-free electrocatalyst for oxygen reduction in fuel cells. *ACS Nano*. 2010;4:1321-1326.
22. Gao K, Wang B, Tao L, et al. Efficient metal-free electrocatalysts from N-doped carbon nanomaterials: mono-doping and co-doping. *Adv Mater*. 2019;31:1805121.
23. Zhao Y, Yang L, Chen S, et al. Can boron and nitrogen co-doping improve oxygen reduction reaction activity of carbon nanotubes? *J Am Chem Soc*. 2013;135:1201-1204.
24. Liu Z, Ma L, Shi G, et al. In-plane heterostructures of graphene and hexagonal boron nitride with controlled domain sizes. *Nat Nanotechnol*. 2013;8:119-124.
25. Du A, Chen Y, Zhu Z, Lu G, Smith SC. C-BN single-walled nanotubes from hybrid connection of BN/C nanoribbons: prediction by ab initio density functional calculations. *J Am Chem Soc*. 2009;131:1682-1683.
26. Peterson AA, Abild-Pedersen F, Studt F, Rossmeisl J, Nørskov JK. How copper catalyzes the electroreduction of carbon dioxide into hydrocarbon fuels. *Energ Environ Sci*. 2010;3:1311-1315.
27. Hong X, Chan K, Tsai C, Nørskov JK. How doped MoS2 breaks transition-metal scaling relations for CO2 electrochemical reduction. *Acs Catal*. 2016;6:4428-4437.
28. Zhao X, Li L, Zhao M. Lattice match and lattice mismatch models of graphene on hexagonal boron nitride from first principles. *J Condens Matter Phys*. 2014;26:095002.
29. Davies A, Albar JD, Summerfield A, et al. Lattice-matched epitaxial graphene grown on boron nitride. *Nano Lett*. 2017;18:498-504.
30. Huang B, Si C, Lee H, et al. Intrinsic half-metallic BN–C nanotubes. *Appl Phys Lett*. 2010;97:043115.
31. Xu T, Zhou Y, Tan X, et al. Creating the smallest BN nanotube from bilayer h-BN. *Adv Funct Mater*. 2017;27:1603897.
32. Kresse G, Furthmuller J. Efficient iterative schemes for ab initio total-energy calculations using a plane-wave basis set. *Phys Rev B*. 1996;54:11169-11186.
33. Kresse G, Furthmuller J. Efficiency of ab-initio total energy calculations for metals and semiconductors using a plane-wave basis set. *Comp Mater Sci*. 1996;6:15-50.
34. Perdew JP, Burke K, Ernzerhof M. Generalized gradient approximation made simple. *Phys Rev Lett*. 1996;77:3865-3868.
35. Perdew JP, Emzerhof M, Burke K. Rationale for mixing exact exchange with density functional approximations. *J Chem Phys*. 1996;105:9982-9985.
36. Grimme S. Semiempirical GGA-type density functional constructed with a long-range dispersion correction. *J Comput Chem*. 2006;27:1787-1799.
37. Hansen HA, Varley JB, Peterson AA, Nørskov JK. Understanding trends in the electrocatalytic activity of metals and enzymes for CO_2 reduction to CO. *J Phys Chem Lett*. 2013;4:388-392.
38. Peterson AA, Nørskov JK. Activity descriptors for CO_2 electroreduction to methane on transition-metal catalysts. *J Phys Chem Lett*. 2012;3:251-258.

SUPPORTING INFORMATION

Additional supporting information may be found online in the Supporting Information section at the end of this article.

How to cite this article: Mao X, Wijethunge D, Zhang L, et al. Metal-free graphene/boron nitride heterointerface for CO_2 reduction: Surface curvature controls catalytic activity and selectivity. *EcoMat*. 2020;2:e12013. https://doi.org/10.1002/eom2.12013